Earth and Planetary Science Letters 617 (2023) 118269

Contents lists available at ScienceDirect

Earth and Planetary Science Letters

journal homepage: www.elsevier.com/locate/epsl

Eruption history of the Columbia River Basalt Group constrained by high-precision U-Pb and $^{40}Ar/^{39}Ar$ geochronology

Jennifer Kasbohm [a,b,*], Blair Schoene [a], Darren F. Mark [c,d], Joshua Murray [a,e], Stephen Reidel [f,1], Dawid Szymanowski [a,g], Dan Barfod [c], Tiffany Barry [h]

[a] Department of Geosciences, Princeton University, Princeton, NJ 08544, USA
[b] Department of Earth & Planetary Sciences, Yale University, New Haven, CT 06511, USA
[c] Isotope Geosciences Unit, Scottish Universities Environmental Research Centre, University of Glasgow, Rankine Avenue, East Kilbride G12 8QQ, UK
[d] Department of Earth and Environmental Science, University of St. Andrews, St Andrews KY16 9AJ, UK
[e] Department of Earth, Atmospheric and Planetary Sciences, Massachusetts Institute of Technology, Cambridge, MA 02139, USA
[f] Pacific Northwest National Laboratory, Richland, WA 99352, USA
[g] Institute of Geochemistry and Petrology, ETH Zürich, 8092 Zürich, Switzerland
[h] School of Geography, Geology and the Environment, University of Leicester, Leicester LE1 7RH, UK

ARTICLE INFO

Article history:
Received 29 March 2023
Received in revised form 20 May 2023
Accepted 8 June 2023
Available online xxxx
Editor: C.M. Petrone

Keywords:
Columbia River Basalt Group
large igneous provinces
U-Pb zircon geochronology
$^{40}Ar/^{39}Ar$ geochronology
zircon geochemistry
Geomagnetic Polarity Timescale

ABSTRACT

Large igneous province volcanism of the Columbia River Basalt Group (CRBG) has been suggested to play a causal role in elevated global temperatures and atmospheric carbon dioxide levels of the Miocene Climate Optimum (MCO). However, assessing the connection between volcanism and warming is dependent upon an accurate and precise chronology for the timing and duration of CRBG emplacement. Building on our previous work (Kasbohm and Schoene, 2018), we present fifteen new high-precision ages, using CA-ID-TIMS U-Pb on zircon and multi-collector $^{40}Ar/^{39}Ar$ on basaltic groundmass, to provide a detailed dual-chronometer timeline for CRBG eruptions. We use both sets of new ages and precise stratigraphic positions of our samples in an integrated Markov Chain Monte Carlo model to calculate average long-term emplacement rates for main-phase CRBG volcanism of 0.2-0.9 km^3/a, with a high likelihood of one prominent hiatus of 60-120 kyr duration occurring after main-phase emplacement. We analyzed trace elements and hafnium isotopes of each dated zircon from CRBG interbeds. The compositions are consistent with both Cascades subduction volcanism and evolved syn-CRBG volcanism proximal to the depositional area. Our age model also yields ages for all magnetic field reversals during the main phase of CRBG emplacement, which can be used to improve calibrations of Miocene paleoclimate records. We find that main-phase CRBG emplacement is coincident with the greatest sustained warmth of the MCO in astronomically-tuned records. Our work shows the power of using both U-Pb and $^{40}Ar/^{39}Ar$ geochronology in an integrated stratigraphic context to assess data reliability and develop the most robust age model possible for large igneous province emplacement.

1. Introduction

Large igneous provinces (LIPs), Earth's most voluminous volcanic events, have punctuated Earth history, leaving evidence for mass extinctions and climatic perturbations in their wake (Ernst and Youbi, 2017). In the past decade, new radioisotope geochronology has yielded robust constraints on the timing, duration, and volumetric rates of eruption for a number of LIPs (Blackburn et al., 2013; Burgess et al., 2017; Schoene et al., 2019; Sprain et al., 2019). However, only a minority of LIPs possess the wide geographic exposure, well-defined stratigraphy, and datable material amenable to detailed geochronological studies (Kasbohm et al., 2021). Here we report new temporal constraints on the Columbia River Basalt Group (CRBG), the youngest and best-preserved LIP, which is a testbed for quantifying the tempo of LIP emplacement through radioisotope geochronology.

The CRBG has been the subject of decades of effort to document its geochemistry, paleomagnetism, and mineralogy, leading to a well-defined volcanostratigraphy comprising five main formations and dozens of individual stratigraphic members, each with area and volume estimates obtained through mapping and coring campaigns (Reidel et al., 2013). The 210,000 km^3 of the CRBG were

* Corresponding author.
E-mail address: jennifer.kasbohm@yale.edu (J. Kasbohm).
[1] Retired.

https://doi.org/10.1016/j.epsl.2023.118269
0012-821X/

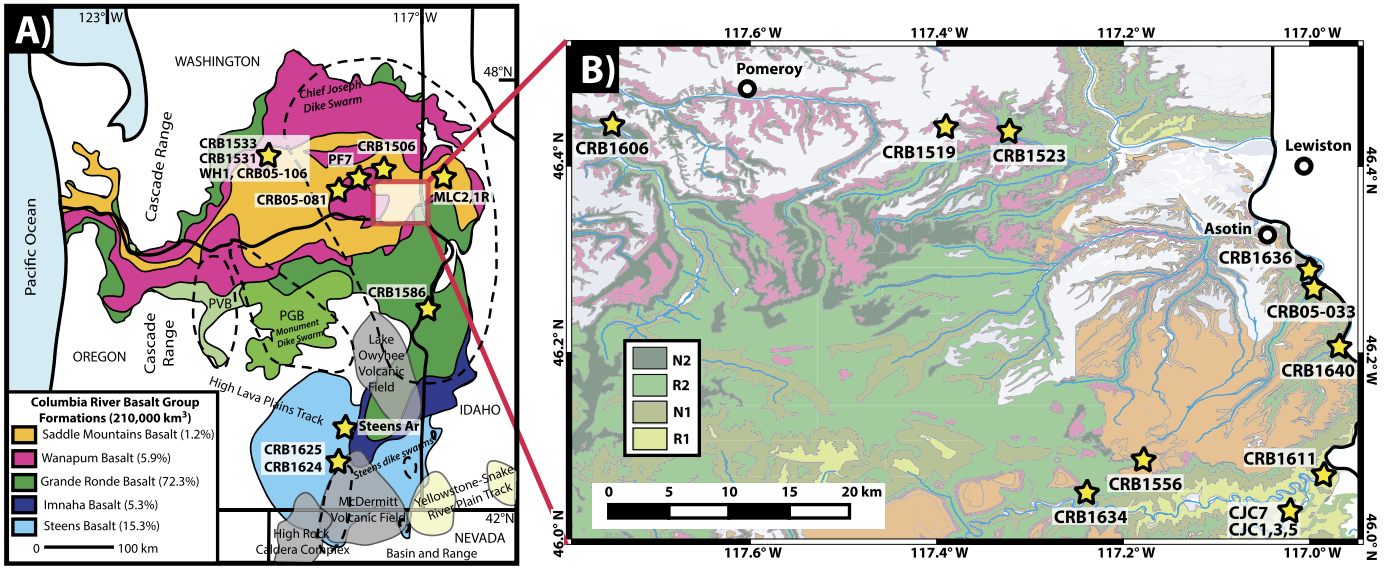

Fig. 1. CRBG Maps. A) Overview map of the CRBG after Reidel et al. (2013) and Kasbohm and Schoene (2018), with areal extents and volume estimates for each formation, localities of regional volcanic activity labeled, and geochronology samples starred. Dashed lines bracket source dike swarms, and the locations of geochronology samples are starred. In total, the Saddle Mountains Basalt, Picture Gorge Basalt (PGB) and Prineville Basalt (PVB) together comprise 2.6% of the total CRBG volume, and are not discussed further here, or included in any cumulative volume estimates. B) Geologic map (Washington State Department of Natural Resources, 2010) of CRBG exposure in southeastern Washington, with geochronology samples starred. We follow Reidel and Tolan (2013a) in using polarity chron abbreviations R1 (the first GRB reversed interval, chron C5Cn.2r), N1 (first normal interval, chron C5Cn.2n), R2 (second reversed interval, chron C5Cn.1r) and N2 (second normal interval, chron C5Cn.1n).

emplaced in western North America during the Miocene, broadly coinciding with active regional volcanism of the Cascades subduction zone to the west, silicic volcanism of the Basin & Range to the south, and the time-progressive silicic eruptive activity of the High Lava Plains and Yellowstone-Snake River Plain hotspot tracks to the south and southeast (Fig. 1A).

The CRBG is noteworthy for its temporal coincidence with the Miocene Climate Optimum (MCO), an episode of global warming at 17-15 Ma evidenced by paleoclimate proxies indicating a 4-6 °C high-latitude sea surface temperature rise (Shevenell et al., 2004) and elevated atmospheric CO_2 levels at or above 600 ppm (Rae et al., 2021). However, prior geochronology for the CRBG lacked the accuracy and precision required to assess in detail its connection to the MCO. Barry et al. (2013) reviewed K-Ar and $^{40}Ar/^{39}Ar$ geochronology obtained from CRBG basalts, and suggested that emplacement of the Steens, Imnaha, Grande Ronde, and Wanapum Basalts (formations; Reidel et al., 2013) occurred between 16.9-15.0 Ma. This age model, constructed from individual ages with low (up to $\sim \pm 1$ Myr, 2σ) precision and in some cases poor accuracy, yielded numerous inconsistencies between the magnetic polarity of the basalts and the Geomagnetic Polarity Timescale (GPTS; Hilgen et al., 2012) (Baksi, 2013).

More recent high-precision $^{40}Ar/^{39}Ar$ and U-Pb zircon geochronology has provided a clearer timeline for CRBG eruptions by dating sanidine or zircon extracted from volcanic ash material between lava flows (Kasbohm and Schoene, 2018; Mahood and Benson, 2017). The U-Pb zircon age model for the CRBG suggested that a portion of the Steens through the Wanapum Basalt was emplaced in ~750 kyr beginning at 16.65 Ma, with possible brief intervals of more rapid emplacement (Kasbohm and Schoene, 2018). Obtaining further high-precision geochronology through the CRBG basalt pile, in particular through the Grande Ronde Basalt (GRB), the largest CRBG formation comprising 72% of its total volume (Reidel et al., 2013), would address uncertainties remaining in the age model and corresponding CRBG eruption rates. The GRB is subdivided into 25 formal and informal stratigraphic members based on geochemistry, mineralogy, and magnetic polarity. Because the GRB was emplaced during two reversed and two normal polarity chrons, individual members are typically grouped into four different informal magnetostratigraphic units: R1 (the first reversed interval, chron C5Cn.2r), N1 (first normal interval, C5Cn.2n), R2 (second reversed interval, C5Cn.1r) and N2 (second normal interval, C5Cn.1n) (Reidel and Tolan, 2013a).

Here, we provide new U-Pb and $^{40}Ar/^{39}Ar$ age constraints on 15 samples from interbeds and basaltic lavas of the CRBG, intercalated with 8 samples dated by Kasbohm and Schoene (2018). These datasets show excellent agreement between chronometers at the ~10 kyr level, permitting integration of these datasets into a single Markov Chain Monte Carlo age model. Our model constrains the eruptive tempo of the CRBG and places tighter age estimates on magnetic reversals observed in the basalt pile, which are critical for building a robust GPTS and subsequent age models for climate proxy records across the MCO. To discern the provenance of the ashbed zircons sampled for U-Pb geochronology, we performed zircon trace element and Hf isotopic analyses that suggest a likely continental arc origin for all CRBG zircons. We show that advances in $^{40}Ar/^{39}Ar$ mass spectrometry, application of Bayesian age models, and a continued progress in assessing systematic uncertainties have the potential to yield a highly resolved record of the timing and tempo of LIP emplacement.

2. Methods

2.1. U-Pb geochronology

We use U-Pb zircon geochronology by chemical abrasion – isotope dilution – thermal ionization mass spectrometry (CA-ID-TIMS) to provide accurate and precise age constraints on CRBG interbeds, as we did in our previous work (Table 1; Kasbohm and Schoene, 2018). Interbeds were sampled from known stratigraphic positions (Fig. 1), and manifest as either ash layers or red weathered lava flow top horizons containing ash material – the latter we identify as "red boles" as they are known in the Deccan Traps (Ghosh et al., 2006; Inamdar and Kumar, 1994). Individual zircons were separated from each sample and dated through CA-ID-TIMS at Princeton University (Table S1; see Supplement for sample descriptions and methods).

Table 1
U-Pb geochronology summary. Location, stratigraphic assignations, and preferred model ages are provided for all U-Pb geochronology samples, with 2σ analytical uncertainty.

Sample	Latitude (°N)	Longitude (°W)	Elevation (m)	Formation: Member, flow over interbed / under interbed	Cumulative Volume (km^3)	Lithology	Preferred Model Age		
							age	Z (2σ)	
								+	−
CRB1506	46.73914	117.75500	470	Wanapum: Priest Rapids, Lolo / Wanapum: Roza	202405	white ash	15.923	0.030	0.031
CRB1533	46.95243	119.99783	227	Upper Vantage (Wanapum: Frenchman Springs, Ginkgo / Grande Ronde: Sentinel Bluffs, Museum (N2))	193719	pumice clasts	16.111	0.049	0.059
CRB1531	46.95243	119.99783	227	Lower Vantage (Wanapum: Frenchman Springs, Ginkgo / Grande Ronde: Sentinel Bluffs, Museum (N2))	192999	white mud	16.134	0.037	0.033
CRB1523	46.43582	117.32221	410	Grande Ronde: Fields Spring (N2)	174904	red bole	16.222	0.046	0.047
CRB1606	46.44399	117.74769	496	Grande Ronde: Fields Spring (N2) / Grande Ronde: Ortley (N2)	172759	breccia infill	16.230	0.045	0.047
CRB1556	46.08543	117.17870	1145	Grande Ronde: Meyer Ridge (R2) / Grande Ronde: Wapshilla Ridge (R2)	150029	red bole	16.260	0.036	0.036
CRB1519	46.44171	117.39066	701	Grande Ronde: Meyer Ridge (R2) / Grande Ronde: Wapshilla Ridge (R2)	150029	red bole	16.260	0.036	0.036
CRB1634	46.05072	117.23906	538	Grande Ronde: Wapshilla Ridge (R2)	109779	red bole	16.327	0.040	0.046
CRB1636	46.28875	116.98751	218	Grande Ronde: Hoskin Gulch (N1)	94004	breccia infill	16.411	0.034	0.035
CRB1640	46.21153	116.96839	271	Grande Ronde: Center Creek (R1)	73254	red bole	16.472	0.048	0.050
CRB1611	46.06924	116.98544	266	Grande Ronde: Buckhorn Springs (R1) / Imnaha: Rock Creek	42800	breccia infill	16.570	0.041	0.044
CRB1586	44.83067	116.90138	641	Imnaha	37300	lapilli tuff	16.601	0.034	0.036
CRB1624	42.66626	118.56479	2966	Upper Steens	31800	breccia infill	16.627	0.033	0.036
CRB1625	42.67542	118.68724	2255	Upper Steens	31500	red bole	16.629	0.032	0.034

Table 2
$^{40}Ar/^{39}Ar$ geochronology summary. Location, stratigraphic assignations, and preferred model ages are provided for all $^{40}Ar/^{39}Ar$ geochronology samples, with 2σ analytical uncertainty.

Sample	Latitude (°N)	Longitude (°W)	Formation: Member, flow	Cumulative Volume (km^3)	Preferred Model Age		
					age	Z (2σ)	
						+	−
DF1	46.56801	118.54468	Wanapum: Roza	202306	15.923	0.031	0.032
PF7	46.66440	118.22414	Wanapum: Frenchman Springs, Silver Falls	195897	15.985	0.072	0.057
CRB05-081	46.50751	118.61615	Wanapum: Eckler Mountain, Dodge	193246	16.133	0.034	0.032
WH1a,b CRB05-106	46.95243	119.99783	Grande Ronde: Sentinel Bluffs (N2), Museum	192900	16.135	0.039	0.033
CRB05-033	46.27222	116.99470	Grande Ronde: Wapshilla Ridge (R2)	129904	16.269	0.036	0.034
MLC2,1R	46.63543	116.61826	Grande Ronde: China Creek (N1)	88604	16.426	0.035	0.034
CJC7	46.02633	117.02167	Grande Ronde: Buckhorn Springs (R1)	43000	16.568	0.042	0.045
CJC1,3,5	46.02633	117.02167	Imnaha	42700	16.571	0.041	0.043
Steens Ar	43.11242	118.27026	Upper Steens	27825	16.640	0.032	0.033

2.2. $^{40}Ar/^{39}Ar$ geochronology

The CRBG lavas are mostly aphyric with notable exceptions in the Steens, Imnaha, Picture Gorge, Wanapum, and Saddle Mountains Basalts. Aphyric lavas require a $^{40}Ar/^{39}Ar$ dating approach that targets groundmass. Nine samples taken from the Steens through Wanapum Basalts were dated using the $^{40}Ar/^{39}Ar$ CO_2 laser step-heating approach. Samples include materials collected during field seasons in 2013 and 2015 (Fig. 1), as well as materials previously $^{40}Ar/^{39}Ar$ dated by Barry et al. (2010) (Table 2). Fresh groundmass was prepared for $^{40}Ar/^{39}Ar$ dating from all samples. In contrast to Barry et al. (2010), who prepared materials as large (mm- to cm-sized) chips/fragments/crystals of whole rock and feldspar that were washed in methanol and de-ionized water, we adopted the rigorous approach of Preece et al. (2018) to produce pristine 125-250 µm fragments of aphyric groundmass. Sample preparation details are provided in the Supplement. $^{40}Ar/^{39}Ar$ ages were calculated using the optimization model of Renne et al. (2011) and the parameters of Renne et al. (2011). All ages are reported at the 2σ confidence interval.

2.3. Zircon trace element geochemistry and Hf isotopes

To explore the origin of CRBG interbed zircons, we performed zircon trace element and Hf isotopic analyses for all zircons dated in Kasbohm and Schoene (2018) and this work. During U-Pb ion exchange chromatography 'wash' fractions were obtained following the 'trace element analysis' (TEA) protocol (Schoene et al., 2010). These fractions consisted of zircon matrix components, including Zr, Hf, minor, and trace elements. Concentrations of these elements in aliquots of ~1/3 of the wash fraction volume were analyzed at Princeton University on a quadrupole inductively coupled plasma mass spectrometer. Hf separations from the remaining solution followed Eddy et al. (2017) and Hf isotopic analyses were performed at Princeton University on a multi-collector inductively coupled plasma mass spectrometer. Methods are detailed in O'Connor et al. (2022) and reproduced in the Supplement, with results in Tables S4 and S5.

3. Results

The sampling of materials from a well-characterized stratigraphic context allows CRBG lava flows dated through $^{40}Ar/^{39}Ar$ geochronology to be placed within stratigraphic order relative to the volcaniclastic units that were sampled for zircon U-Pb geochronology. As such, a composite section with samples taken at known values of cumulative volume can be utilized for age modeling (Tables 1 and 2). To assign cumulative volumes to our samples, we used the volumes of Reidel et al. (2013), reproduced in Ta-

ble S6. A sample collected between two members was assigned a cumulative volume above the entirety of the lower member; a sample collected in a member was assigned the cumulative volume in the middle of that member, unless we had further information about its proximity to the upper or lower contact.

3.1. U-Pb geochronology results

Individual zircon $^{206}Pb/^{238}U$ dates from fourteen CRBG interbed horizons are presented in Fig. 2 with 95% confidence intervals; six new GRB samples are shown alongside our prior dataset (Kasbohm and Schoene, 2018). Dates within each sample spread beyond analytical uncertainty as a result of prolonged pre-eruptive crystallization in the magma, or inheritance of older grains from the host rock or volcanic edifice (Cooper, 2015; Miller et al., 2007; Simon et al., 2008). In Kasbohm and Schoene (2018), we used the youngest precise zircon date as our best estimate for the age of the interbed. To more robustly calculate an eruption age from dispersed zircon dates, in this study each sample was subjected to a Bayesian Markov Chain Monte Carlo (MCMC) model, which makes a probabilistic estimate of eruption age based on all of the individual zircon dates and their analytical uncertainties, and uses informed priors about the true distribution of zircon crystallization before eruption (Keller et al., 2018). In all cases, the derived eruption ages overlap with the youngest zircon ages yet are less precise (Fig. 2, Table S2). Finally, eruption ages were input into an additional MCMC simulation (Schoene et al., 2019), which imposes stratigraphic order as a constraint to further refine eruption ages, and calculates volumetric eruption rates (Fig. 3). We have revised the stratigraphic position of sample CRB1625 from Kasbohm and Schoene (2018); this sample was taken from the Upper rather than the Lower Steens Basalt and is of normal rather than reversed polarity (V. Camp, personal communication).

3.2. $^{40}Ar/^{39}Ar$ geochronology results

Forty-eight aliquots of nine samples were $^{40}Ar/^{39}Ar$ dated. All samples yield plateau ages consistent with the criteria of Schaen et al. (2021). Data are presented in Fig. 4 with isotope correlation plots presented in Table S3. All 48 plateaus define inverse isochrons with initial $^{40}Ar/^{36}Ar$ trapped components indistinguishable from atmospheric argon (Mark et al., 2011) and ages indistinguishable from the plateau ages. Up to 9 aliquots of each sample were analyzed to maximize analytical precision. Systematic uncertainties were propagated into the weighted average age for each individual sample. Analytical precision (2σ) ranges from 0.24–0.38% with total systematic precision ranging from 0.27–0.41%. All sample ages adhere to stratigraphic younging.

The analytical precision achieved by this study shows an order of magnitude improvement relative to data reported by Barry et al. (2010) and represents a significant improvement in precision relative to other $^{40}Ar/^{39}Ar$ studies of the CRBG (reviewed in Baksi, 2013; Barry et al., 2013) due to the meticulous sample preparation detailed above and our experimental approach. While Barry et al. (2010) utilized a single-collector MAP 215-50 noble gas mass spectrometer, we utilized a multi-collector noble gas mass spectrometer (ARGUS V) (Mark et al., 2009). Analysis of 20 mg aliquots of material allowed for 15 step experiments to tease apart the variable argon reservoirs within the samples to recover relatively high radiogenic ^{40}Ar plateau steps. Importantly, the multi-aliquot approach has also allowed us to drive down internal uncertainties through replication and reproducibility of the data. As such, the 2σ systemic uncertainty for each sample is of the same order of magnitude as the 2σ systematic uncertainty for U-Pb ages.

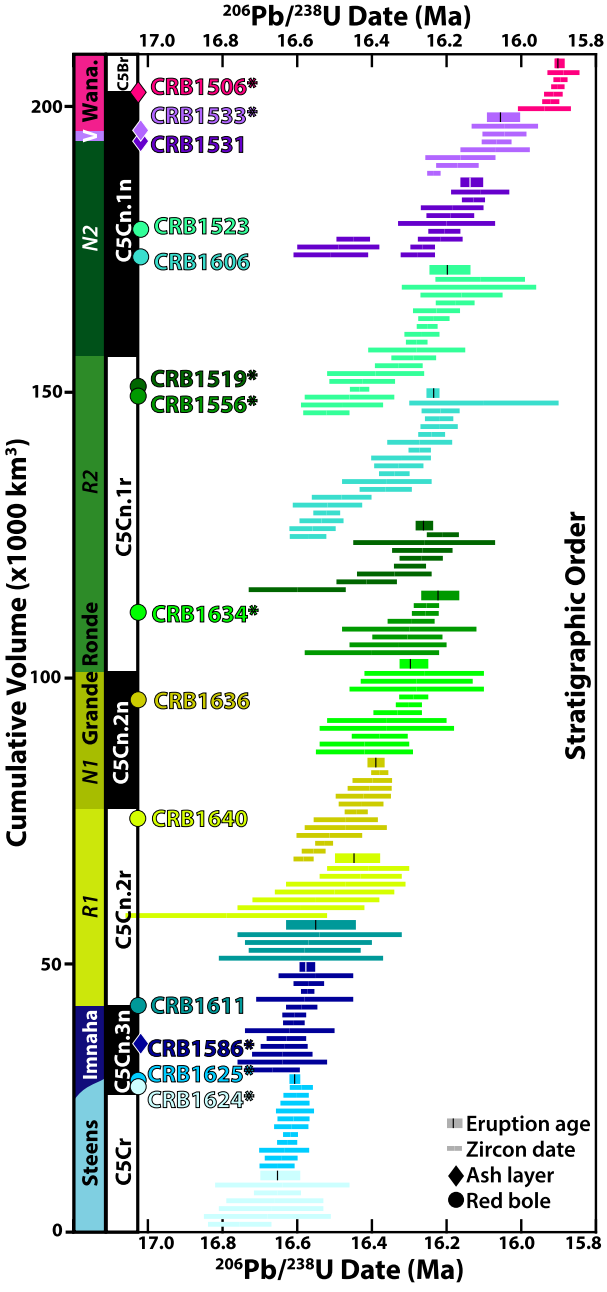

Fig. 2. U-Pb zircon CA-ID-TIMS geochronological data. Rank order plot of U-Pb geochronological data presented in this study, with each bar representing an individual zircon analysis, and analyses from each sample are grouped by color. Samples are arranged in stratigraphic order (younging bottom to top), and the width of each bar shows 2σ uncertainty. The result of our Bayesian zircon eruptive age modeling after Keller et al. (2018) (median and 95% credible interval) is highlighted (the top bar for each sample) and represents the input used in our Markov Chain Monte Carlo superposition age model. Samples with an asterisk are from Kasbohm and Schoene (2018). The columns on the left indicate the stratigraphic position and cumulative volume estimate for each sample, as well as CRBG magnetostratigraphy. The position of the Vantage sedimentary interbed is labeled with "V".

3.3. CRBG eruption rates

Our geochronological data yield a high-resolution age model for the vast majority of the CRBG that agrees well with our previous U-Pb age estimates. We show excellent agreement between U-Pb and $^{40}Ar/^{39}Ar$ age estimates of the timing of each eruptive member of the CRBG, allowing us to leverage our results into an integrated dual-chronometer age model (Fig. 5) that modifies the modeling approach of Schoene et al. (2019) to account for systematic uncer-

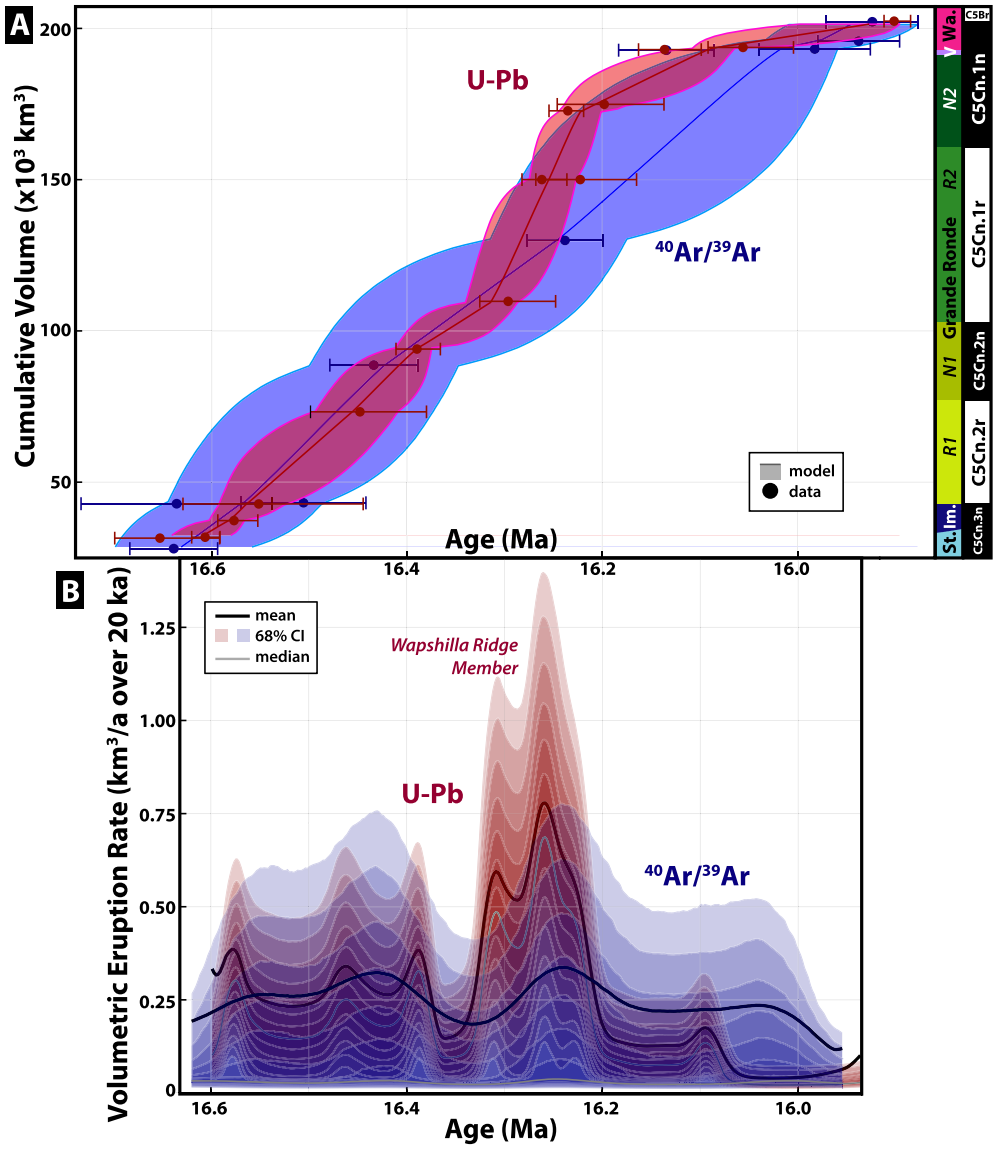

Fig. 3. CRBG U-Pb and $^{40}Ar/^{39}Ar$ age models. A) U-Pb (red) and $^{40}Ar/^{39}Ar$ (blue) age models for cumulative volume erupted through the CRBG. Input data for the models are U-Pb eruptive ages after Keller et al. (2018) and $^{40}Ar/^{39}Ar$ dates with 2σ analytical uncertainty. Shading indicates 95% credible interval of the models, with internal uncertainties only. The position of the Vantage sedimentary interbed is labeled with "V". B) Results from (A) were used in further MCMC simulation to calculate average long-term emplacement rates through the eruptive history of the CRBG, averaged over 20 kyr windows, shown with contours up to the 68% credible interval (CI).

tainties in each method (details in the Supplement). We use the outputs of this dual-chronometer model to calculate all ages and durations (with full systematic, 2σ uncertainties), quoted here as our preferred interpretation.

Our age model allows for a more thorough interrogation of the GRB. Interbeds immediately below the first, and above the last, GRB members – both of which were dated through $^{40}Ar/^{39}Ar$ geochronology – robustly constrain the duration of the GRB to 458+38/−42 kyr. The age model yields estimates for the timing of the magnetic field reversals bracketing the four magnetostratigraphic units of the GRB as well as the preceding and subsequent chrons (Table 3). Ages for the bottom, and near the top, of the Vantage sedimentary interbed (labeled in purple as V in Figs. 2, 3, and 5), the most prominent though not necessarily the longest-lived interbed in the CRBG (Barry et al., 2010), yield a duration of 57+84/−44 kyr.

Our dual-chronometer age model (Fig. 5) calculates an average long-term emplacement rate of ~0.3 km^3/a for the Steens, Imnaha, and the first half of the GRB. More rapid emplacement of up to ~0.9 km^3/a occurs during the Wapshilla Ridge Member, in chron C5Cn.1r (R2). Fluxes slow drastically during the emplacement of the Wanapum Basalt, with rates slowing to $\leq$0.1 km^3/a. Because our ages indicate relatively continuous eruptions, we were interested in determining the timing and duration of the longest possible hiatus within the CRBG, prior to the Saddle Mountains Basalt (see Supplement). We queried each run of our dual-chronometer model, and we find that the longest hiatus was most likely 60-120 kyr duration (Fig. S5), during early stages of Wanapum Basalt emplacement, and likely coincident with deposition of the Vantage interbed. Since the Vantage interbed is underlain by the Basalt of Museum (Sentinel Bluffs Member, GRB) and overlain by the Basalt of Ginkgo (Frenchman Springs Member, Wanapum Basalt), Vantage deposition was likely coeval with early Wanapum Basalt members (e.g., Eckler Mountain) (Table S6). This result is consistent with our calculated low eruption rate for the Wanapum Basalt.

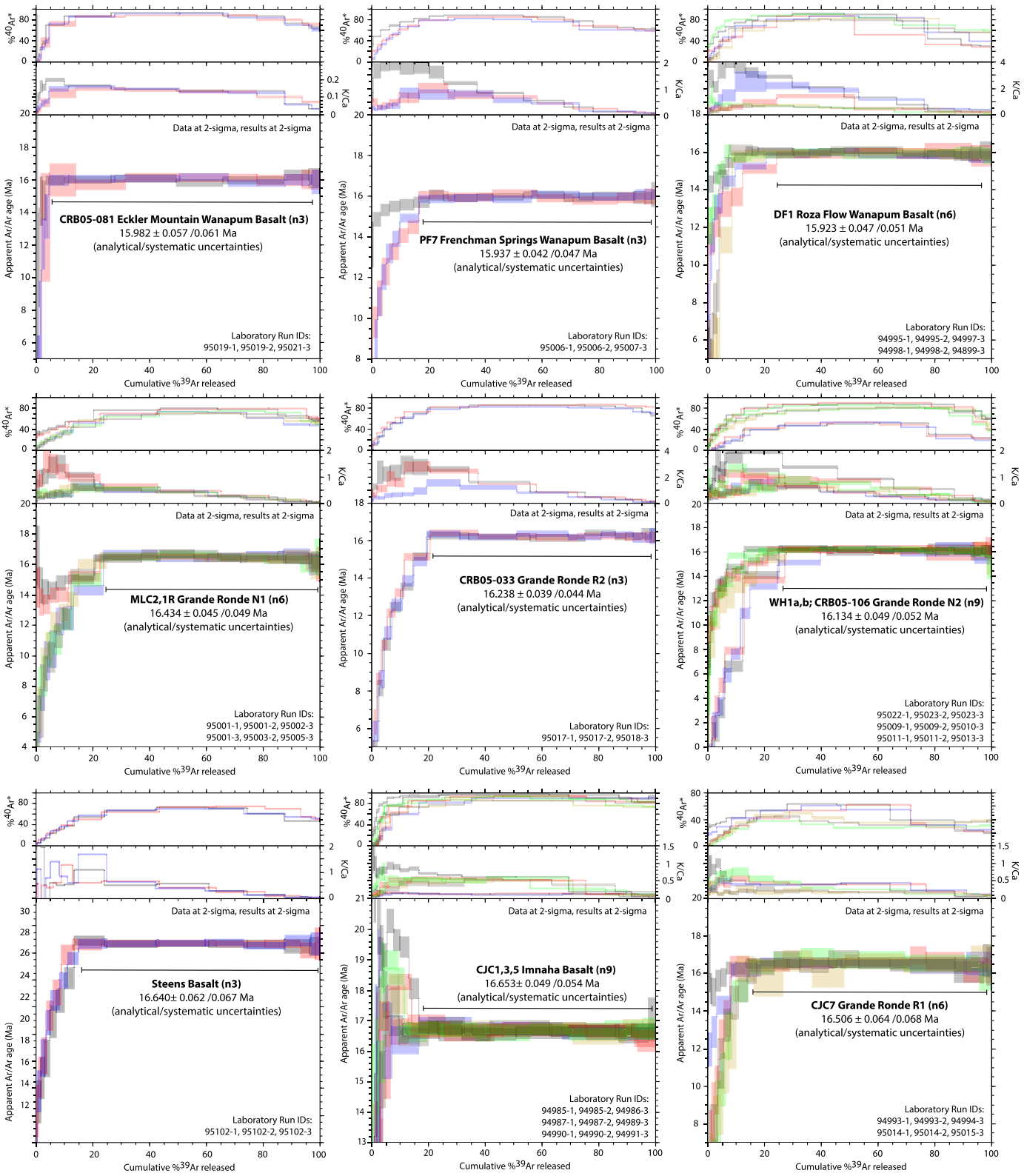

Fig. 4. ^{40}Ar/^{39}Ar data. ^{40}Ar/^{39}Ar age spectra showing multiple aliquots for each sample. Data and results are shown at the 2σ uncertainty, weighted average age ± analytical/systematic uncertainty. Associated isotope correlation plots are shown in Table S3.

3.4. Zircon geochemistry and Hf isotopes of CRBG interbeds

At the sample level, CRBG interbed zircons exhibit somewhat variable Hf isotope and trace element compositions but show no clear stratigraphic or age-based trends (Fig. 6). For the most part, within individual samples, zircons tend to exhibit similar εHf and rare earth element (REE) ratios (e.g., Lu/Gd). Zircons from the two Upper Steens Basalt interbed samples have similar εHf and Lu/Gd composition, but different age spectra, indicating that they may be from the same volcanic system; zircons from the overly-

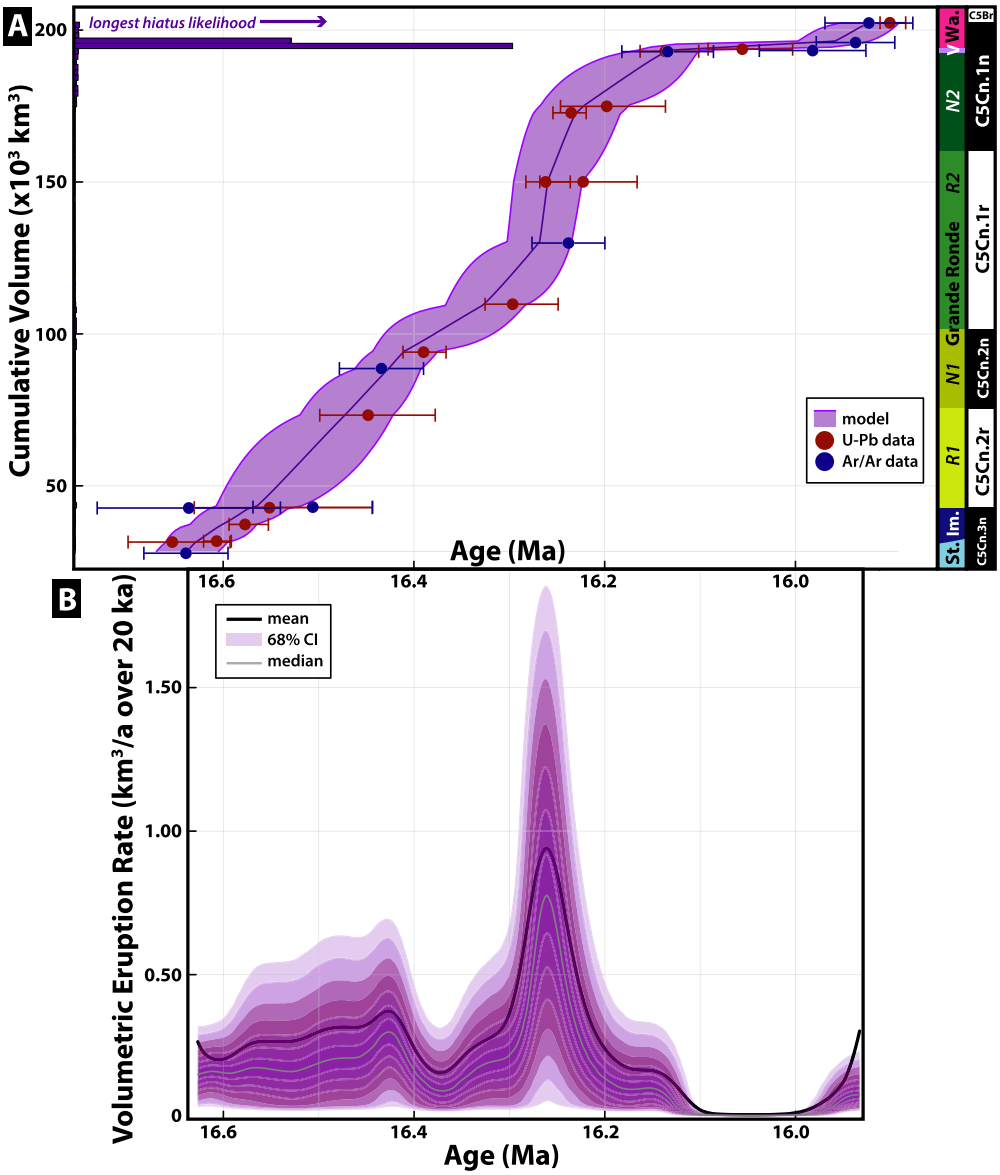

Fig. 5. CRBG dual-chronometer age model. A) Dual chronometer age model for cumulative volume erupted through the CRBG. Input data for the models are U-Pb eruptive ages after Keller et al. (2018) and $^{40}Ar/^{39}Ar$ dates with 2σ analytical uncertainty. Shading indicates 95% credible interval of the models, incorporating full systematic uncertainties. Indigo bars on the left indicate the likelihood of the longest CRBG hiatus (most likely 60-120 kyr) occurring at each stratigraphic position. The age model also yields magnetic field reversal and formation boundary ages. The position of the Vantage sedimentary interbed is labeled with "V". B) Results from (A) for average long-term emplacement rates through the eruptive history of the CRBG, averaged over 20 kyr windows, shown with contours up to 68% credible intervals (CI).

ing Imnaha Basalt interbed samples overlap with some individual Steens zircons, but show slightly higher εHf values. Zircons from GRB interbeds exhibit greater variability than the other formations in both εHf and Lu/Gd, including within specific samples. Vantage interbed zircons show lower εHf than those erupted during the main-phase CRBG, while Wanapum Basalt interbed sample CRB1506 yielded zircons with higher Lu/Gd than the main-phase CRBG. There is no obvious trend of increasing or decreasing εHf or REE ratios through time or by sample – while CRB1506 is an outlier in every plot, its zircon Hf concentrations of >15,000 ppm and U concentrations of >4000 ppm indicate that zircons crystallized from a highly evolved melt (Grimes et al., 2015). Its offset from other samples in Figs. 6–7 is therefore indicative of a compositional extreme, rather than a temporal evolution. The εHf and REE ratios of most of the ash samples also overlap with many red bole samples, with no discernible offset based on the observed lithology of these samples. Other zircon trace element concentrations are plotted in Figs. 7 and S7 after Grimes et al. (2015) to discern the origin of these zircons, and are interpreted in section 4.2.

4. Discussion

4.1. A new dual-chronometer high-precision age model for the CRBG

Using nine $^{40}Ar/^{39}Ar$ and fourteen U-Pb ages, we construct a dual-chronometer age model for the CRBG, from the Upper Steens through the Wanapum Basalts (Fig. 5). Samples young upward stratigraphically in our integrated dataset when compared with both analytical (X) and systematic inter-chronometer (Z) uncertainties, representing a marked improvement in the accuracy and precision of CRBG age data over that obtained in prior work (Baksi, 2013; Barry et al., 2013). While Baksi (2022) reported 15 new ages from the GRB and Wanapum Basalts, and works to bring these ages in concordance with the U-Pb data of Kasbohm and Schoene (2018) and legacy calibrations of the GPTS, we identify several dif-

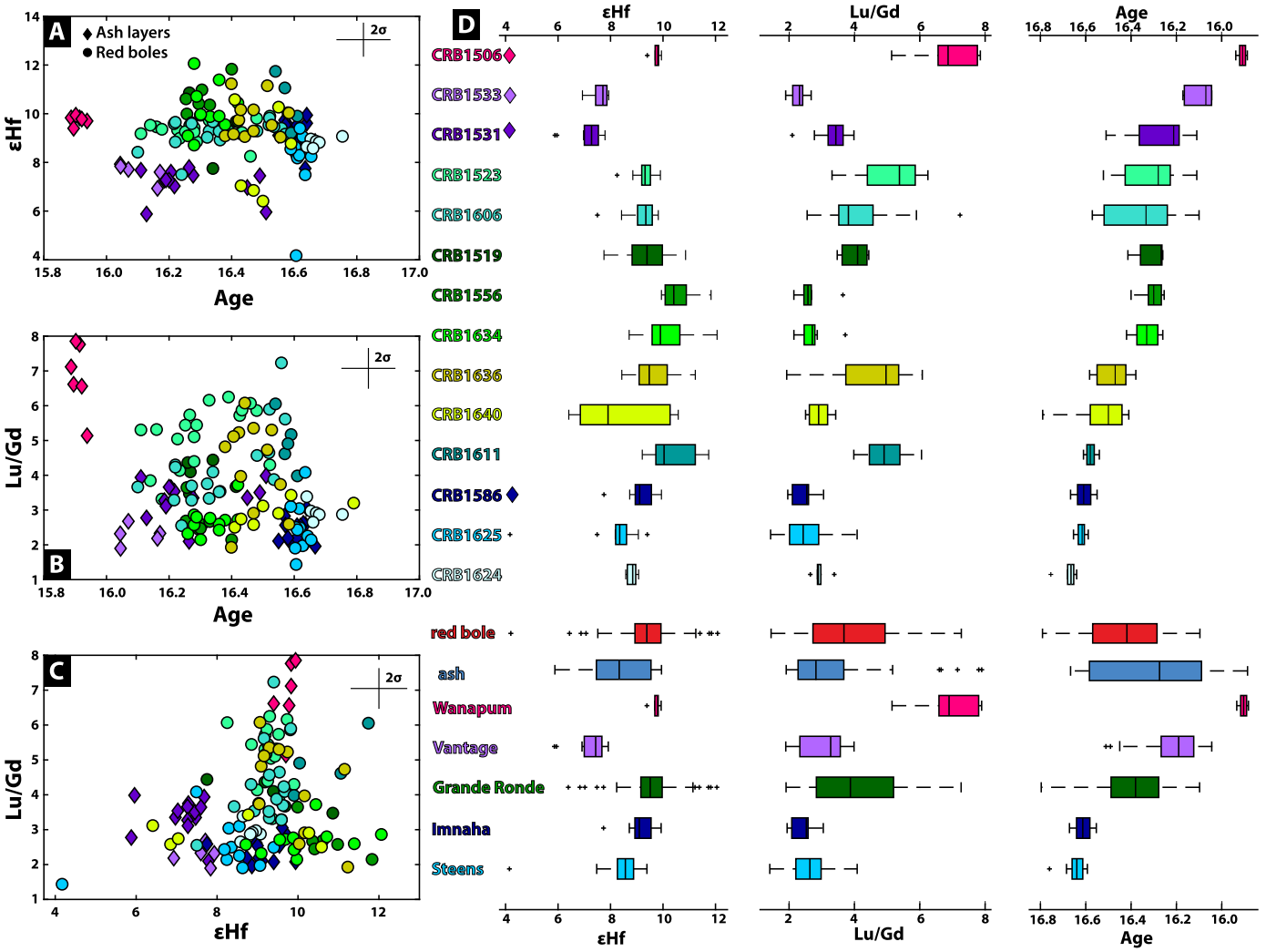

Fig. 6. CRBG zircon geochemistry. Results from TIMS-TEA and hafnium isotope analysis of all interbed zircons dated in the CRBG. Lu/Gd was chosen as a representative rare earth element ratio. A) εHf versus zircon age; depleted mantle εHf value is ~+16, which is outside the range of the plot. B) Lu/Gd versus zircon age. C) Lu/Gd versus εHf. D) Box and whisker plots visualizing the data displayed in A-C, with values grouped by sample, lithology (red bole versus ash layer), and CRBG formation.

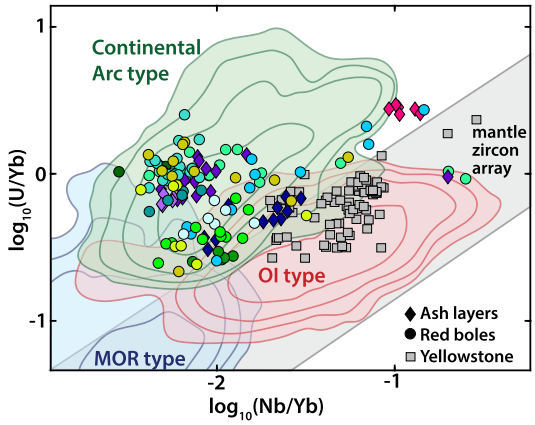

Fig. 7. CRBG zircon provenance. Tectono-magmatic zircon provenance diagram after Grimes et al. (2015), outlining fields for mid-ocean ridge (MOR type), ocean island and other plume-influenced (OI type), and continental arc type zircons. CRBG zircons analyzed are color-coded by sample, with lithology identified by shape, and are compared to ~100 ka zircons analyzed from Yellowstone volcanics by Stelten et al. (2013).

ferent methodological approaches in the Supplement that lead us to prefer our new dual-chronometer age model.

The only exception to the pattern of younging upward is $^{40}Ar/^{39}Ar$ samples CJC-1,3,5 in the Imnaha Basalt, which yielded a weighted average age of 16.653±0.049 Ma (X) that overlaps with ages in both datasets for the Steens Basalt. We have previously suggested that the Steens and Imnaha Basalts were emplaced simultaneously (Kasbohm and Schoene, 2018), further evidenced by stratigraphic observations and paleomagnetic data (Camp et al., 2013; Hooper et al., 2002). We recognize that the relative order of emplacement of U-Pb sample CRB1586 and CJC-1,3,5 is uncertain, as the Imnaha Basalt is not as granularly subdivided as the GRB. While CRB1586 was collected between two Imnaha lava flows in sequence with others (leading a cumulative volume estimate central to the formation), CJC-1,3,5 were taken from an Imnaha Basalt flow that immediately underlies the Imnaha/GRB contact, leading us to believe it was deposited towards the end of Imnaha emplacement.

Considered with respect to the U-Pb data, the Imnaha $^{40}Ar/^{39}Ar$ weighted average age may not be representative of an eruption age. Low temperature steps in the age spectra of some of the Imnaha Basalt aliquots show excess Ar release with ages dropping from approximately 20 Ma in the first 20% ^{39}Ar release to define an apparent coherent age plateau at 16.653 Ma (Table S3). The inverse isochrons show that these plateau steps define initial trapped Ar components consistent with atmosphere, but with rela-

Table 3
Geomagnetic Polarity Timescale calibration. Using our CRBG age model and the stratigraphic position/cumulative volume of each magnetic field reversal, we provide here ages for polarity chron onsets and chron durations during CRBG emplacement, reported with 95% credible intervals. We compare our reversal ages to astronomically tuned age models from Sites U1335 and U1336 (Channell et al., 2013; Kochhann et al., 2016; Ohneiser et al., 2013), Site 1090 (Billups et al., 2004), Site 154 (Pälike et al., 2006), and the spline fit based on magnetic seafloor anomalies from the Astronomically Tuned Neogene Timescale (ATNTS) in Geologic Time Scale 2012 (Hilgen et al., 2012). We find the greatest agreement between our model and the tuning results of Kochhann et al. (2016) from Site U1336, which provides the calibration for this portion of the Miocene in GTS 2020 (Raffi et al., 2020).

Polarity Chron Onset	CRBG Reversal Age Model (Dual-Chronometer, Z)					Other GPTS Calibrations					Reversal Age Differences				
	Cumulative Volume (km^3)	Reversal Age (Ma)	Maximum Reversal Age (Ma)	Minimum Reversal Age (Ma)	Chron Duration (ka)	U1335 Tuned Age (Ma)	GTS 2020: U1336 Tuned Age (Ma)	1090 Tuned Age (Ma)	154 Tuned Age (Ma)	ATNTS 2012 Spline Age (Ma)	Δ CRBG Age - U1335 Age (Ma)	Δ CRBG Age - U1336 Age (Ma)	Δ CRBG Age - 1090 Age (Ma)	Δ CRBG Age - 154 Age (Ma)	Δ CRBG Age - ATNTS 2012 Age (Ma)
C5Br*	202405	15.923	15.952	15.891	-	15.896	15.994	15.898	15.899	15.974	agrees	−0.042	agrees	agrees	−0.022
C5Cn.1n	157659	16.251	16.290	16.206	335+25/−24	16.242	16.261	16.161	16.162	16.268	agrees	agrees	0.045	0.04392	agrees
C5Cn.1r	101629	16.370	16.426	16.310	108+48/−48	16.34	16.351	16.255	16.256	16.303	agrees	agrees	0.054653	0.05365	0.007
C5Cn.2n	77004	16.461	16.511	16.412	99+55/−56	16.415	16.434	16.318	16.319	16.472	agrees	agrees	0.093935	0.09294	agrees
C5Cn.2r	42800	16.570	16.612	16.527	107+44/−45	16.514	16.532	16.405	16.406	16.543	0.013	agrees	0.121567	0.12057	agrees
C5Cn.3n	23850	16.651	16.683	16.620	72+44/−35	16.582	16.637	16.498	16.499	16.721	0.038	agrees	0.121764	0.12076	−0.0384

* Minimum age estimate.

tively large uncertainties owing to clustering of data on the isotope correlation plot. It is possible that some of these aliquots have not adequately deconvolved the radiogenic ^{40}Ar from an excess ^{40}Ar component on the age spectra and the age for this sample is inaccurate. The youngest aliquot from this batch shows no evidence of excess Ar release in the low temperature steps and defines an age of 16.636±0.098 Ma with the oldest aliquot and evidence of excess Ar release in the low T steps defining an age of 16.660±0.094 Ma. On this basis, we propose the youngest single aliquot $^{40}Ar/^{39}Ar$ age for the Imnaha Basalt is the most appropriate age constraint for this eruption, rather than a weighted mean of all aliquots.

Our $^{40}Ar/^{39}Ar$ ages are calculated using the calibration of the Fish Canyon sanidine (FCs) from Renne et al. (2011). In Fig. S6 we compare these results and our U-Pb age model to an alternative $^{40}Ar/^{39}Ar$ age model using the FCs calibration of Kuiper et al. (2008) with full systematic uncertainties. We show good agreement between all three calibrations, though the Kuiper FCs $^{40}Ar/^{39}Ar$ age model results in sample ages that are younger by ∼55 kyr and have larger overall systematic uncertainties, inflating the sample $^{40}Ar/^{39}Ar$ ages by at least ∼26 ka. However, owing to the robust uncertainty propagation associated with the optimization model, we move forward with the FCs calibration of Renne et al. (2011) (see Supplement for further discussion).

Considered separately (Fig. 3), our $^{40}Ar/^{39}Ar$ and U-Pb age models show excellent agreement in the average long-term CRBG emplacement rate of ∼0.3 km^3/a through the Steens, Imnaha, and early GRB. In the latter GRB and Wanapum Basalt, the shapes of the eruptive curves differ slightly, though they still overlap. The apparent difference in rates can be explained by the fact that the $^{40}Ar/^{39}Ar$ age model has only two samples in the interior of the GRB to calibrate effusion rates (in N1 and R2); the other two GRB samples in the model are at the top and bottom contacts of the formation. By contrast, the U-Pb model provides ages at the top and bottom of the Wapshilla Ridge Member and in the central portion of overlying N2 lava flows, allowing for the resolution of a pulse of volcanism during Wapshilla Ridge emplacement, followed by slower rates during N2. Without samples in the middle of N2, our $^{40}Ar/^{39}Ar$ age model cannot capture these changes and also misses the hiatus during the deposition of the Vantage interbed, which effectively smooths out the eruption rate history suggested by our U-Pb age model. However, the overlap between our age models in Fig. 3 also leaves open the possibility for nearly complete agreement between our techniques, a significant advance in the application of geochronology to LIPs, which we take one step further by integrating both datasets into our dual-chronometer model (Fig. 5). Our preferred integrated model captures both the Wapshilla Ridge pulse and the Vantage hiatus, robustly constraining the emplacement history of the CRBG. Ideally, future studies of LIPs that undertake a dual-chronometer approach could be designed from the start to aim for sample coverage evenly spaced throughout the stratigraphy using both techniques, which also provides a check on the reliability of both datasets.

Although our age model suggests an average long-term emplacement rate for the CRBG of 0.2-0.9 km^3/a, we recognize the crucial difference between this rate calculation and the timescales of the emplacement of individual lava flows. Studies suggesting that individual CRBG lava flows may have been emplaced in as little as ∼1 month (Reidel et al., 2018 and references therein) indicate that much of the eruptive history of the CRBG may have been characterized by pauses in volcanism, that we cannot resolve with the ∼10-50 kyr precision of geochronology. Thermal models (Petcovic and Dufek, 2005) combined with thermochronologic data (Karlstrom et al., 2019) have been used to show that feeder dike segments were active for at most 1-10 years with fluxes of 1-3 km^3/yr. Using a magnetic geothermometer, Biasi and Karlstrom (2021) have also shown that dike segments were active for months

to years, with emplacement rates as high as 1-8 km^3/day sustained over several years. We agree with Biasi and Karlstrom (2021) that the rapid emplacement of individual eruptions would have had a severe environmental effect that is likely underestimated in climate models thus far.

Our model for average long-term volumetric emplacement rates throughout the duration of the CRBG may be compared to other well-dated LIPs. U-Pb ID-TIMS geochronology shows that the CAMP, Deccan Traps, and Siberian Traps were also all emplaced in less than a million years, with age models suggesting 10-100 kyr-long periods of high eruptive flux interspersed with intervals of reduced effusion (Kasbohm et al., 2021). The Deccan Traps emplacement is shown to occur in four pulses of $\leq$20 km^3/a (Schoene et al., 2019); the Siberian Traps have been modeled to be emplaced as a few pulses lasting 10-100 kyr (Pavlov et al., 2019). In the CAMP, some U-Pb dates from dikes and sills fall during apparent eruption hiatuses (Blackburn et al., 2013; Davies et al., 2017), perhaps indicating that in all LIPs, lulls in eruptions need not be lulls in magmatism. More detailed geochronology is needed to assess whether apparent eruption hiatuses in some LIPs are simply a transition to intrusion-dominated magmatism or regional phenomena and an artifact of incomplete sampling. In contrast to other LIPs with multiple potential hiatuses of ~100 kyr, we model one eruption hiatus during CRBG emplacement that was unlikely to be longer than 60-120 kyr. The gradual, rather than pulsed, emplacement rate of the CRBG, as well as its smaller total volume – less than or equal to the volume of just one Deccan Traps pulse – may partly explain why the CRBG is not associated with the more catastrophic environmental and ecological effects of other LIPs.

4.2. Provenance of CRBG interbed zircons

We obtained hafnium isotopes and trace element concentrations from all CRBG interbed zircons dated for U-Pb geochronology with the goals of discerning zircon provenance and better understanding how these interbeds formed. While zircon trace elements may vary within a single eruptive center (e.g., Claiborne et al., 2018), hafnium isotopes are considered more indicative of source magma composition (e.g., Vervoort and Blichert-Toft, 1999). The cross-plot of Lu/Gd and εHf in Fig. 6C shows some grouping of samples of similar or varying ages, which could indicate that each group is sourced from airfall from distinct eruptive centers that may have erupted multiple times. These groups include CRB1624 and 1625; CRB1634 and 1556; and CRB1519, 1606, and 1636. CRB1640, with the widest spread in εHf, overlaps with each of these groups, potentially indicating multiple sources for its zircons (Fig. 6D). These groups are located in distinct regions of the CRBG, bolstering our interpretation that zircons were sourced from distinct eruptive centers; we would expect more uniformly scattering distributions if all red bole zircons were detrital. The offset in εHf values for Vantage zircons in samples CRB1531 and CRB1533 clearly indicate a different source magma from the other CRBG zircons. The geographic position of Vantage west of the rest of the samples, and the lithological interpretation of the interbed as a Cascades volcaniclastic lahar (Reidel and Tolan, 2013b; Tolan et al., 2009) support this interpretation. Apart from these offsets, there is no systematic difference in the chemistry of zircons sourced from red boles or ash layers - zircons from both lithologies overlap, even when erupted at different times (such as CRB1586 and CRB1634). We thereby interpret all zircons from both red bole and ash layer lithologies to be of magmatic rather than detrital origin and suggest that red boles incorporate volcaniclastic airfall sourced from regional volcanism. This interpretation is bolstered by the excellent agreement between our U-Pb ages for interbeds and $^{40}Ar/^{39}Ar$ ages on adjacent lava flows.

Grimes et al. (2015) interpreted trace element ratios in zircon to aid in the determination of the tectono-magmatic setting that allowed for zircon crystallization. The most diagnostic of these, U/Yb vs Nb/Yb (Fig. 7), shows that nearly all CRBG zircons fall in the continental arc-type field. The most parsimonious interpretation for most, if not all U-Pb CRBG interbeds sampled is that they are composed wholly or in part of volcaniclastic material sourced from the Cascades arc, with positive εHf values of these zircons indicative of a source dominated by juvenile, radiogenic mantle-derived material with modest involvement of old lithospheric sources. Volcanic products of Pacific Northwest arc magmatism, from the Cretaceous accreted arc terranes (Sauer et al., 2017) through the Eocene onset of Cascades subduction to the Quaternary (Jicha et al., 2009), exhibit εHf values from +8 to +12, overlapping with values obtained for most CRBG interbed zircons. The position of all zircons from ashbed sample CRB1586, interbedded with the Imnaha Basalt, and red bole samples CRB1634 and CRB1556, interbedded with the GRB, are in the portion of the continental arc field that overlies the ocean island-type field. These samples may alternatively be sourced from plume-related evolved-composition magmatism that occurred simultaneously with the emplacement of the CRBG. To assess this possibility and compare our results with products of mantle plume magmatism, we plot trace element data from much younger ~100 ka Yellowstone zircons (Stelten et al., 2013) on Fig. 7. Almost all plot in the ocean island (plume-type) region; CRB1586 is our only sample that overlaps with Yellowstone trace element values. Three zircons from CRB1531 and CRB1523 plot only in the ocean island-type field but possess ages and εHf values that overlap with other zircons in these samples that are in the continental arc field, indicating a similar provenance even if trace elements are somewhat offset. While some ash beds in the Saddle Mountains Basalt have been linked to the Cougar Point Tuff from the Bruneau-Jarbridge eruptive center in the Yellowstone hotspot track (Nash and Perkins, 2012), the zircon trace element chemistry we report here, in addition to substantially younger ages for Yellowstone hotspot volcanism, lead us to reject a similar mechanism of emplacement for main-phase CRBG interbeds.

Our preferred interpretation for the origin of pre-Saddle Mountains CRBG interbeds and their zircons is deposition of volcaniclastic material due to ongoing Cascades subduction volcanism, or more directly genetically-related, evolved syn-CRBG volcanism more proximal to the depositional area (e.g., the Columbia River Rhyolites recently described by Streck et al. (2023)). Despite some overlapping trace element chemistry, CRBG zircons are offset in εHf values from younger Yellowstone-Snake River Plain zircons which have values below 0, a consequence of their parental magmas developing within cratonic lithosphere east and south of CRBG outcrop area (Colón et al., 2018; Ellis et al., 2019; Stelten et al., 2013). The εHf values from CRBG interbed zircons overlap with whole-rock εHf values obtained from the Picture Gorge Basalts (Stefano et al., 2019) and zircon εHf values for the Dinner Creek Tuff (Colón et al., 2015). The Dinner Creek Tuff is interbedded with the Basalts of Malheur Gorge and Hunter Creek (Streck et al., 2015), which have previously been suggested to be correlative with the GRB (Barry et al., 2013); common εHf values between this unit and CRBG interbed zircons may suggest a similar magmatic source. Stefano et al. (2019) present whole-rock basalt εHf values for the Picture Gorge Basalt of +10 to +12, which overlap values obtained for CRB1634 and CRB1556. Since zircons from these CRBG interbeds also plot in the region of Fig. 7 where the continental arc and ocean island fields overlap, these zircons could plausibly have crystallized from magmas evolved through closed-system differentiation of CRBG-like melts. Meanwhile, Camp et al. (2013) report εHf values of +10 to +12 for whole-rock Steens and Imnaha Basalts, but our Hf isotope analyses of interbeds from these

formations yielded lower values of +7 to +10, suggesting that a differentiation mechanism may not be universally applicable.

4.3. Geologic time scale and paleoenvironmental implications

Using our highly resolved CRBG age model, we can probe the connection of the CRBG with the MCO. One obstacle to comparing the timing of the CRBG with the MCO has been the disputed calibration of the Miocene GPTS, for which there have been several proposals. Our new CRBG U-Pb age model gives ages for the onsets of polarity chrons C5Cn.3n through C5Br, with an average uncertainty of ±40 kyr. Although we now recognize that CRB1625 is from the Upper Steens Basalt, and therefore our samples do not bracket the onset of chron C5Cn.3n, our age model dates it to 16.651+0.032/−0.031 Ma. The new CRBG age model confirms our previous observation (Kasbohm and Schoene, 2018) that magnetic field reversal ages in the CRBG show greater concordance with the astronomically-tuned age model for magnetic field reversals in IODP site U1336 (Kochhann et al., 2016) than with either the prior calibration of the Neogene GPTS in Geologic Timescale 2012 (Hilgen et al., 2012) or other astronomically-tuned GPTS calibrations from Sites 1090 and 154 (Billups et al., 2004; Pälike et al., 2006) (Table 3). This insight was cited in Geologic Timescale 2020 (Raffi et al., 2020) to bolster the adoption of reversal ages between ∼18-15 Ma from Site U1336 as the new 2020 GPTS calibration. The timing of the onset we resolve for chron C5Cn.3n is substantially offset from all other calibrations apart from Site U1336.

Raffi et al. (2020) observed that the largest offset between the CRBG reversal ages documented by Kasbohm and Schoene (2018) and in Site U1336 occurs for chron C5Br, which has an astronomically tuned age of 15.994 Ma. Even with our new CRBG age model, this offset persists, though with a decreased magnitude; we report an $^{40}Ar/^{39}Ar$ age of 15.923+0.031/−0.032 Ma for the transitionally-magnetized Roza Member, and a U-Pb model age of 15.923+0.030/−0.031 Ma for an ash overlying this Member, which was likely deposited after the reversal was completed. The tuned age for this reversal may violate stratigraphic superposition, since it precedes both of these ages as well as potentially our $^{40}Ar/^{39}Ar$ age for the underlying-normally magnetized Basalt of Silver Falls at 15.985+0.072/−0.057 Ma (Table S6). The C5Br reversal age of 15.994 Ma from Site U1336 also exhibits the greatest magnitude of offset in this time interval from the same chron boundary at neighboring Site U1335, dated to 15.896 Ma, which agrees well with our radiometric ages. We therefore suggest that the younger chron age from U1335 be adopted for the age of C5Br. This evaluation shows the importance of utilizing both tuning and geochronology to assess the timing of magnetic field reversals and gain a full understanding of sedimentation in tuned sections (e.g., Sahy et al., 2017). An accurate GPTS is essential to anchor the paleoclimate proxy records that document critical events in Earth's climate history, like the MCO.

A motivating question for our work has been to assess the temporal correlation between the CRBG and the MCO; our new results bolster the correlation documented by Kasbohm and Schoene (2018). Though we lack a sample in the Lower Steens Basalt, given the fairly constant average emplacement rate we present here, it seems unlikely that Steens Basalt eruptions began earlier than 16.9-16.75 Ma (assuming constant emplacement rates of 0.1-0.2 km^3/yr). With samples in and above the Roza Member, we show that Wanapum Basalt eruptions mostly concluded by ∼15.9 Ma. Meanwhile, a compilation of astronomically tuned records of the Cenozoic suggests that the onset of MCO warming, signified by the decline in benthic foraminiferal $\delta^{18}O$, occurred 17.0-16.9 Ma, and that low $\delta^{18}O$ values persisted until ∼14.5 Ma (Westerhold et al., 2020). We note that in Sites U1337 (Holbourn et al., 2015) and U1336 (Kochhann et al., 2016), the longest sustained interval of the lowest $\delta^{18}O$ values occurs from ∼16.9-16.0 Ma, coincident with the main phase of CRBG volcanism. Similarly, a foraminiferal $\delta^{11}B$ isotope proxy for MCO atmospheric CO_2 concentrations show a brief increase at ∼16.7 Ma, followed by sustained elevated levels from ∼16.5-15.8 Ma (Sosdian et al., 2018). If the age models for these records are accurate, these patterns permit a connection between an increase in global temperatures, pCO_2 and main-phase CRBG magmatism.

A key question remaining in discerning the role of the CRBG in the MCO is the relative order of warming and surface volcanism. Our prior work (Kasbohm and Schoene, 2018) had suggested that Steens Basalt emplacement began ∼16.7 Ma, 200 kyr after astronomically-tuned calibrations for MCO warming (Westerhold et al., 2020), but our new age model suggests an earlier onset for Steens volcanism, either beginning synchronously with the MCO at 16.9 Ma, or postdating the MCO onset by ∼125 kyr. While a potential offset may seem to suggest another more important driving factor for the MCO than LIP volcanism, a new study modeling subsurface sill emplacement of the CRBG shows that intrusive emplacement would have released enormous quantities of CO_2 ∼200 kyr prior to surface volcanism, with modeled temperatures during sill emplacement matching those observed during the MCO (Tian and Buck, 2022). Such a mechanism may have allowed for the CRBG to play a causal role in the MCO if the onset of warming occurred prior to volcanism. Further studies that temporally constrain climatic fluctuations through the duration of the MCO, the onset of CRBG volcanism, and initial sill emplacement will allow testing of this possibility.

Our geochronology conclusively shows that all but ∼1% of CRBG eruptions had ceased by ∼15.9 Ma, and therefore, the CRBG cannot be invoked as a source of CO_2 through the entire duration of the MCO. In a carbon cycle modeling study undertaken to discern the connection between the MCO, CRBG, and the concurrent Monterey Carbon Isotope Excursion, Sosdian et al. (2020) suggest that elevated surface ocean dissolved inorganic carbon (DIC) throughout the MCO was caused by continuous eruption of the CRBG over millions of years, citing an outdated age model of CRBG emplacement rates (Hooper et al., 2002). Since our new CRBG age model constrains the timing of the main phase of volcanism to ∼16.8-15.9 Ma, with eruptive fluxes at least 10 times that of Hooper et al. (2002), we suggest that another mechanism of sustaining elevated DIC and seawater temperatures through this interval must be invoked after 15.9 Ma. One scenario is that elevated crustal geotherms sustained decarbonation reactions of carbon-rich sediments long after CRBG magmatism ceased, although such sediments are minor relative to the mostly cratonic and volcanic country rock in the eruptive area of the CRBG (Reidel et al., 2013). Another possible mechanism is a potentially slower silicate weathering feedback allowing for sustained warm conditions following the cessation of main phase CRBG volcanism, although a slight increase in $\delta^{18}O$ values and decrease in pCO_2 estimates after ∼15.8 Ma is consistent with a responsive weathering feedback. Both explanations require better data on the magnitude of each effect, especially since they may explain carbon cycle observations during other examples of LIP emplacement and environmental change, such as mass extinction events (e.g., Ruhl and Kürschner, 2011).

4.4. Benefits of a dual-chronometer approach and remaining systematic uncertainties

Our work represents the first time that $^{40}Ar/^{39}Ar$ ages for CRBG lavas have shown excellent agreement with U-Pb ages, and the first time that these techniques have been not only juxtaposed (as in Baksi, 2022) but fully integrated in a single study to produce an age model for a LIP. After decades of effort to reduce systematic uncertainties in the U-Pb and $^{40}Ar/^{39}Ar$ geochronome-

ters along with improvements in measurement technologies, we can now obtain high-fidelity datasets that allow for resolution of time distributed within LIPs. Within LIPs no one chronometer can date all geologic processes of interest, but we demonstrate through strategic deployment of a dual-chronometer approach and an interpretive frameworks built on geologic observations that events can be resolved at the 10 kyr level. The $^{40}Ar/^{39}Ar$ data show that within the CRBG, the high-precision interbed U-Pb zircon data track eruption histories, supported by zircon geochemistry consistent with a volcanic provenance. The independent U-Pb chronology has highlighted a potential issue with the weighted mean $^{40}Ar/^{39}Ar$ age for the Imnaha Basalt. We also show that both geochronology systems can contribute to calibrating the Miocene GPTS and bolster calibrations derived from astronomical tuning. Ultimately, the $^{40}Ar/^{39}Ar$ and U-Pb communities need to continue probing technique-specific systematic uncertainties to resolve the up to 0.4% offset between techniques, but that offset is now small enough that as long as $^{40}Ar/^{39}Ar$ data of suitable precision are collected, the communities can come together to collect and interrogate high fidelity dual-chronometer data.

5. Conclusion

Our new high-precision U-Pb and $^{40}Ar/^{39}Ar$ age model for the CRBG offers a uniquely detailed view of the dynamics of LIP emplacement. Our concordant geochronological data for the CRBG from both techniques demonstrates that 83% of the total volume of the CRBG (bracketed by our Upper Steens $^{40}Ar/^{39}Ar$ sample, and our U-Pb sample overlying the Roza Member) was emplaced in ~720 ka. The GRB, representing 72% of total CRBG volume, was emplaced over 458+38/−42 kyr. The longest hiatus that occurred during our modeled interval was most likely 60-120 kyr in duration, in the early stages of Wanapum Basalt emplacement. New trace element and hafnium isotope geochemistry from CRBG interbed zircons suggest a magmatic, continental arc provenance for these grains, indicating that interbeds contain volcaniclastic material that record primary eruptive ages. The volumetric emplacement rates of 0.2-0.9 km^3/yr calculated through the main phase of CRBG volcanism likely contributed to its differing environmental effects from other LIPs; rather than association with a cataclysmic mass extinction, the CRBG instead was likely partly responsible for establishing the conditions of the MCO. Our work highlights the importance of integrating multiple high-precision chronometers to present the most highly resolved age models possible for LIP emplacement.

CRediT authorship contribution statement

Jennifer Kasbohm: Conceptualization, Formal analysis, Funding acquisition, Investigation, Visualization, Writing – original draft, Writing – review & editing. **Blair Schoene:** Conceptualization, Formal analysis, Funding acquisition, Investigation, Methodology, Resources, Supervision, Writing – review & editing. **Darren F. Mark:** Conceptualization, Investigation, Resources, Visualization, Writing – original draft, Writing – review & editing. **Joshua Murray:** Investigation, Writing – review & editing. **Stephen Reidel:** Resources, Supervision, Writing – review & editing. **Dawid Szymanowski:** Investigation, Methodology, Writing – review & editing. **Dan Barfod:** Investigation, Writing – review & editing. **Tiffany Barry:** Resources, Writing – review & editing.

Declaration of competing interest

The authors declare that they have no known competing financial interests or personal relationships that could have appeared to influence the work reported in this paper.

Data availability

All data is available in supplemental files. Code may be requested from the authors.

Acknowledgements

The authors thank B. Martin and V. Camp for assistance defining the stratigraphic position of our geochronology samples. S. Bartusek, K. Duffey, and L. O'Connor provided able assistance in the lab and field. S. Gibson and an anonymous reviewer are thanked for their constructive reviews of this manuscript, which also benefited from a previous review by M. Schmitz and suggestions from C.B. Keller. J.K. thanks D. Suwondo for personal and logistical support, and S. Gorthala for effective co-working. This material is based upon work supported by the National Science Foundation Graduate Research Fellowship under grant no. DGE-1656466, the National Science Foundation under Awards No. 1952753 and 1735512, by Princeton Environmental Institute at Princeton University through the Walbridge Fund, and by the Princeton University Department of Geosciences Scott Vertebrate Fund.

Appendix A. Supplementary material

Supplementary material related to this article can be found online at https://doi.org/10.1016/j.epsl.2023.118269.

References

Baksi, A.K., 2013. Timing and duration of volcanism in the Columbia River Basalt Group: a review of existing radiometric data and new constraints on the age of the Steens through Wanapum Basalt extrusion. Spec. Pap., Geol. Soc. Am. 497 (03), 67–85. https://doi.org/10.1130/2013.2497(03).

Baksi, A.K., 2022. New 40Ar/39Ar ages from the Grande Ronde and Wanapum Basalt, Columbia River Basalt Group (CRBG): compilation of all ages and relationship to the geomagnetic polarity time scale for ~17–15 Ma. J. Earth Syst. Sci. 131 (3), 158. https://doi.org/10.1007/s12040-022-01892-3.

Barry, T.L., Self, S., Kelley, S.P., Reidel, S.P., Hooper, P.R., Widdowson, M., 2010. New $^{40}Ar/^{39}Ar$ dating of the Grande Ronde lavas, Columbia River Basalts, USA: implications for duration of flood basalt eruption episodes. Lithos 118 (3–4), 213–222. https://doi.org/10.1016/j.lithos.2010.03.014.

Barry, T.L., Kelley, S.P., Camp, V.E., Self, S., Jarboe, N.A., Duncan, R.A., 2013. Eruption chronology of the Columbia River Basalt Group. Spec. Pap., Geol. Soc. Am. 497, 45–66. https://doi.org/10.1130/2013.2497(02).

Biasi, J., Karlstrom, L., 2021. Timescales of magma transport in the Columbia River flood basalts, determined by paleomagnetic data. Earth Planet. Sci. Lett. 576, 117169. https://doi.org/10.1016/j.epsl.2021.117169.

Billups, K., Pälike, H., Channell, J.E.T., Zachos, J.C., Shackleton, N.J., 2004. Astronomic calibration of the late Oligocene through early Miocene geomagnetic polarity time scale. Earth Planet. Sci. Lett. 224 (1–2), 33–44. https://doi.org/10.1016/j.epsl.2004.05.004.

Blackburn, T.J., Olsen, P.E., Bowring, S.A., McLean, N.M., Kent, D.V., Puffer, J.H., et al., 2013. Zircon U-Pb geochronology links the end-Triassic extinction with the Central Atlantic magmatic Province. Science. https://doi.org/10.1126/science.1234204.

Burgess, S.D., Muirhead, J.D., Bowring, S.A., 2017. Initial pulse of Siberian Traps sills as the trigger of the end-Permian mass extinction. Nat. Commun. 8 (1), 164. https://doi.org/10.1038/s41467-017-00083-9.

Camp, V.E., Ross, M.E., Duncan, R.A., Jarboe, N.A., Coe, R.S., Hanan, B.B., Johnson, J.A., 2013. The Steens Basalt: earliest lavas of the Columbia River Basalt Group. Spec. Pap., Geol. Soc. Am. 497 (4), 87–116. https://doi.org/10.1130/2013.2497(04).

Channell, J.E.T., Ohneiser, C., Yamamoto, Y., Kesler, M.S., 2013. Oligocene-Miocene magnetic stratigraphy carried by biogenic magnetite at sites U1334 and U1335 (equatorial Pacific Ocean). Geochem. Geophys. Geosyst. 14, 265–282. https://doi.org/10.1029/2012GC004429.

Claiborne, L.L., Miller, C.F., Gualda, G.A., Carley, T.L., Covey, A.K., Wooden, J.L., Fleming, M.A., 2018. Zircon as magma monitor: robust, temperature-dependent partition coefficients from glass and zircon surface and rim measurements from natural systems. In: Moser, D.E., Corfu, F., Darling, J.R., Reddy, S.M., Tait, K. (Eds.), Microstructural Geochronology: Planetary Records Down to Atom Scale, 1st ed., pp. 3–33.

Colón, D.P., Bindeman, I.N., Stern, R.A., Fisher, C.M., 2015. Isotopically diverse rhyolites coeval with the Columbia River Flood Basalts: evidence for mantle plume interaction with the continental crust. Terra Nova 27 (4), 270–276. https://doi.org/10.1111/ter.12156.

Colón, D.P., Bindeman, I.N., Wotzlaw, J.F., Christiansen, E.H., Stern, R.A., 2018. Origins and evolution of rhyolitic magmas in the central snake river plain: insights from coupled high-precision geochronology, oxygen isotope, and hafnium isotope analyses of zircon. Contrib. Mineral. Petrol. 173 (2), 1–18. https://doi.org/10.1007/s00410-017-1437-y.

Cooper, K.M., 2015. Timescales of crustal magma reservoir processes: insights from U-series crystal ages. Geol. Soc. Spec. Publ. 422 (1), 141–174. https://doi.org/10.1144/SP422.7.

Davies, J.H.F.L., Marzoli, A., Bertrand, H., Youbi, N., Ernesto, M., Schaltegger, U., 2017. End-Triassic mass extinction started by intrusive CAMP activity. Nat. Commun. 8, 15596. https://doi.org/10.1038/ncomms15596.

Eddy, M.P., Jagoutz, O., Ibañez-Mejia, M., 2017. Timing of initial seafloor spreading in the Newfoundland-Iberia rift. Geology 45 (6), 527–530. https://doi.org/10.1130/G38766.1.

Ellis, B.S., Schmitz, M.D., Hill, M., 2019. Reconstructing a Snake River Plain 'super-eruption' via compositional fingerprinting and high-precision U/Pb zircon geochronology. Contrib. Mineral. Petrol. 174 (12). https://doi.org/10.1007/s00410-019-1641-z.

Ernst, R.E., Youbi, N., 2017. How Large Igneous Provinces affect global climate, sometimes cause mass extinctions, and represent natural markers in the geological record. Palaeogeogr. Palaeoclimatol. Palaeoecol. 478, 30–52. https://doi.org/10.1016/j.palaeo.2017.03.014.

Ghosh, P., Sayeed, M.R.G., Islam, R., Hundekari, S.M., 2006. Inter-basaltic clay (bole bed) horizons from Deccan traps of India: implications for palaeo-weathering and palaeo-climate during Deccan volcanism. Palaeogeogr. Palaeoclimatol. Palaeoecol. 242 (1–2), 90–109. https://doi.org/10.1016/j.palaeo.2006.05.018.

Grimes, C.B., Wooden, J.L., Cheadle, M.J., John, B.E., 2015. "Fingerprinting" tectonomagmatic provenance using trace elements in igneous zircon. Contrib. Mineral. Petrol. 170 (5–6), 46. https://doi.org/10.1007/s00410-015-1199-3.

Hilgen, F.J., Lourens, L.J., Van Dam, J.A., Beu, A.G., Boyes, A.F., Cooper, R.A., et al., 2012. Chapter 29 - The Neogene period. In: The Geologic Time Scale 2012, 2-Volume Set. https://doi.org/10.1016/B978-0-444-59425-9.00029-9.

Holbourn, A., Kuhnt, W., Kochhann, K.G.D., Andersen, N., Sebastian Meier, K.J., 2015. Global perturbation of the carbon cycle at the onset of the Miocene Climatic Optimum. Geology 43 (2), 123–126. https://doi.org/10.1130/G36317.1.

Hooper, P.R., Binger, G.B., Lees, K.R., 2002. Ages of the Steens and Columbia River flood basalts and their relationship to extension-related calc-alkalic volcanism in eastern Oregon. Bull. Geol. Soc. Am. 114 (1), 43–50. https://doi.org/10.1130/0016-7606(2002)114<0043:AOTSAC>2.0.CO;2.

Inamdar, P.M., Kumar, D., 1994. On the origin of bole beds in Deccan Traps. J. Geol. Soc. India 44 (3), 331–334.

Jicha, B.R., Hart, G.L., Johnson, C.M., Hildreth, W., Beard, B.L., Shirey, S.B., Valley, J.W., 2009. Isotopic and trace element constraints on the petrogenesis of lavas from the Mount Adams volcanic field, Washington. Contrib. Mineral. Petrol. 157 (2), 189–207. https://doi.org/10.1007/s00410-008-0329-6.

Karlstrom, L., Murray, K.E., Reiners, P.W., 2019. Bayesian Markov-Chain Monte Carlo inversion of low-temperature thermochronology around two 8 – 10 m Wide Columbia River Flood Basalt Dikes. Front. Earth Sci. 7. https://doi.org/10.3389/feart.2019.00090.

Kasbohm, J.J., Schoene, B., 2018. Rapid eruption of the Columbia River flood basalt and correlation with the mid-Miocene climate optimum. Sci. Adv. 4 (9), 1–8. https://doi.org/10.1126/sciadv.aat8223.

Kasbohm, J.J., Schoene, B., Burgess, S.D., 2021. Radiometric constraints on the timing, tempo, and effects of large igneous province emplacement. In: Ernst, R.E., Dickson, A.J., Bekker, A. (Eds.), Large Igneous Provinces: A Driver of Global Environmental and Biotic Changes. American Geophyiscal Union and John Wiley and Sons, Inc., pp. 27–82.

Keller, C.B., Schoene, B., Samperton, K.M., 2018. A stochastic sampling approach to zircon eruption age interpretation. Geochem. Perspect. Lett., 31–35. https://doi.org/10.7185/geochemlet.1826.

Kochhann, K.G.D., Holbourn, A., Kuhnt, W., Channell, J.E.T., Lyle, M., Shackford, J.K., et al., 2016. Eccentricity pacing of eastern equatorial Pacific carbonate dissolution cycles during the Miocene Climatic Optimum. Paleoceanography 31 (9), 1176–1192. https://doi.org/10.1002/2016PA002988.

Kuiper, K.F., Deino, A.L., Hilgen, F.J., Krijgsman, W., Renne, P.R., Wijbrans, J.R., 2008. Synchronizing Rock Clocks of Earth History. Science 320 (5875), 500–504. https://doi.org/10.1126/science.1154339.

Mahood, G.A., Benson, T.R., 2017. Using $^{40}Ar/^{39}Ar$ ages of intercalated silicic tuffs to date flood basalts: precise ages for Steens Basalt Member of the Columbia River Basalt Group. Earth Planet. Sci. Lett. 459, 340–351. https://doi.org/10.1016/j.epsl.2016.11.038.

Mark, D.F., Barfod, D., Stuart, F.M., Imlach, J., 2009. The ARGUS multicollector noble gas mass spectrometer: performance for $^{40}Ar/^{39}Ar$ geochronology. Geochem. Geophys. Geosyst. 10 (2), 1–9. https://doi.org/10.1029/2009GC002643.

Mark, D.F., Stuart, F.M., de Podesta, M., 2011. New high-precision measurements of the isotopic composition of atmospheric argon. Geochim. Cosmochim. Acta 75 (23), 7494–7501. https://doi.org/10.1016/j.gca.2011.09.042.

Miller, J.S., Matzel, J.E.P., Miller, C.F., Burgess, S.D., Miller, R.B., 2007. Zircon growth and recycling during the assembly of large, composite arc plutons. J. Volcanol. Geotherm. Res. 167 (1–4), 282–299. https://doi.org/10.1016/j.jvolgeores.2007.04.019.

Nash, B.P., Perkins, M.E., 2012. Neogene Fallout Tuffs from the Yellowstone Hotspot in the Columbia Plateau Region, Oregon, Washington and Idaho, USA. PLoS ONE 7 (10). https://doi.org/10.1371/journal.pone.0044205.

Ohneiser, C., Acton, G., Channell, J.E.T., Wilson, G.S., Yamamoto, Y., Yamazaki, T., 2013. A middle Miocene relative paleointensity record from the Equatorial Pacific. Earth Planet. Sci. Lett. 374, 227–238. https://doi.org/10.1016/j.epsl.2013.04.038.

Pälike, H., Frazier, J., Zachos, J.C., 2006. Extended orbitally forced palaeoclimatic records from the equatorial Atlantic Ceara Rise. Quat. Sci. Rev. 25 (23–24), 3138–3149. https://doi.org/10.1016/j.quascirev.2006.02.011.

Pavlov, V.E., Fluteau, F.F., Latyshev, A.V., Fetisova, A.M., Elkins-Tanton, L.T., Black, B.A., et al., 2019. Geomagnetic secular variations at the permian-Triassic boundary and pulsed magmatism during eruption of the Siberian traps. Geochem. Geophys. Geosyst. 20 (2). https://doi.org/10.1029/2018GC007950.

Petcovic, H.L., Dufek, J.D., 2005. Modeling magma flow and cooling in dikes: implications for emplacement of Columbia River flood basalts. J. Geophys. Res., Solid Earth 110 (10), 1–15. https://doi.org/10.1029/2004JB003432.

Preece, K., Mark, D.F., Barclay, J., Cohen, B.E., Chamberlain, K.J., Jowitt, C., et al., 2018. Bridging the gap: $^{40}Ar/^{39}Ar$ dating of volcanic eruptions from the "Age of Discovery". Geology 46 (12), 1035–1038. https://doi.org/10.1130/G45415.1.

Rae, J.W.B., Zhang, Y.G., Liu, X., Foster, G.L., Stoll, H.M., Whiteford, R.D.M., 2021. Atmospheric CO_2 over the past 66 million years from marine archives. Annu. Rev. Earth Planet. Sci. 49, 609–641. https://doi.org/10.1146/annurev-earth-082420-063026.

Raffi, I., Wade, B.S., Pälike, H., 2020. The Neogene period. In: Gradstein, F.M., Ogg, J.G., Schmitz, M.D., Ogg, G.M. (Eds.), Geologic Time Scale 2020, vol. 2. Elsevier B.V., pp. 1141–1215.

Reidel, S.P., Tolan, T.L., 2013a. The Grande Ronde Basalt, Columbia River Basalt Group. Spec. Pap., Geol. Soc. Am. 497 (05), 117–153. https://doi.org/10.1130/2013.2497(05).

Reidel, S.P., Tolan, T.L., 2013b. The late Cenozoic evolution of the Columbia River system in the Columbia River flood basalt province. In: Reidel, S.P., Camp, V.E., Ross, M.E., Wolff, J.A., Martin, B.S., Tolan, T.L., Wells, R.E. (Eds.), The Columbia River Flood Basalt Province. In: Geological Society of America Special Paper, vol. 497. Geological Society of America, pp. 201–230.

Reidel, S.P., Camp, V.E., Tolan, T.L., Martin, B.S., 2013. The Columbia River flood basalt province: stratigraphy, areal extent, volume, and physical volcanology. Spec. Pap., Geol. Soc. Am. 497 (1), 1–43. https://doi.org/10.1130/2013.2497(01).

Reidel, S.P., Tolan, T.L., Camp, V.E., 2018. Columbia River flood basalt flow emplacement rates—fast, slow, or variable? In: Poland, M.P., Garcia, M.O., Camp, V.E., Grunder, A. (Eds.), Field Volcanology: A Tribute to the Distinguished Career of Don Swanson, pp. 1–19.

Renne, P.R., Balco, G., Ludwig, K.R., Mundil, R., Min, K., 2011. Response to the comment by W.H. Schwarz et al. on "Joint determination of ^{40}K decay constants and $^{40}Ar^*/^{40}K$ for the Fish Canyon sanidine standard, and improved accuracy for $^{40}Ar/^{39}Ar$ geochronology" by P.R. Renne et al. (2010). Geochim. Cosmochim. Acta 75 (17), 5097–5100. https://doi.org/10.1016/j.gca.2011.06.021.

Ruhl, M., Kürschner, W.M., 2011. Multiple phases of carbon cycle disturbance from large igneous province formation at the Triassic-Jurassic transition. Geology 39 (5), 431–434. https://doi.org/10.1130/G31680.1.

Sahy, D., Condon, D.J., Hilgen, F.J., Kuiper, K.F., 2017. Reducing disparity in radio-isotopic and astrochronology-based time scales of the Late Eocene and Oligocene. Paleoceanography 32 (10), 1018–1035. https://doi.org/10.1002/2017PA003197.

Sauer, K.B., Gordon, S.M., Miller, R.B., Vervoort, J.D., Fisher, C.M., 2017. Evolution of the Jura-Cretaceous North American Cordilleran margin: insights from detrital-zircon U-Pb and Hf isotopes of sedimentary units of the North Cascades Range, Washington. Geosphere 13 (6), 2094–2118. https://doi.org/10.1130/GES01501.1.

Schaen, A.J., Jicha, B.R., Hodges, K.V., Vermeesch, P., Stelten, M.E., Mercer, C.M., et al., 2021. Interpreting and reporting $^{40}Ar/^{39}Ar$ geochronologic data. Geol. Soc. Am. Bull. 133 (3-4), 461–487. https://doi.org/10.1130/b35560.1.

Schoene, B., Latkoczy, C., Schaltegger, U., Günther, D., 2010. A new method integrating high-precision U–Pb geochronology with zircon trace element analysis (U–Pb TIMS-TEA). Geochim. Cosmochim. Acta 74 (24), 7144–7159. https://doi.org/10.1016/j.gca.2010.09.016.

Schoene, B., Eddy, M.P., Samperton, K.M., Keller, C.B., Keller, G., Adatte, T., Khadri, S.F.R., 2019. U-Pb constraints on pulsed eruption of the Deccan Traps across the end-Cretaceous mass extinction. Science 363 (6429), 862–866. https://doi.org/10.1126/science.aau2422.

Shevenell, A.E., Kennett, J.P., Lea, D.W., 2004. Middle miocene Southern Ocean cooling and Antarctic cryosphere expansion. Science 305, 1766–1770. https://doi.org/10.1126/science.1100061.

Simon, J.I., Renne, P.R., Mundil, R., 2008. Implications of pre-eruptive magmatic histories of zircons for U-Pb geochronology of silicic extrusions. Earth Planet. Sci. Lett. 266 (1–2), 182–194. https://doi.org/10.1016/j.epsl.2007.11.014.

Sosdian, S.M., Greenop, R., Hain, M.P., Foster, G.L., Pearson, P.N., Lear, C.H., 2018. Constraining the evolution of Neogene ocean carbonate chemistry using the boron isotope pH proxy. Earth Planet. Sci. Lett. 498, 362–376. https://doi.org/10.1016/j.epsl.2018.06.017.

Sosdian, S.M., Babila, T.L., Greenop, R., Foster, G.L., Lear, C.H., 2020. Ocean Carbon Storage across the middle Miocene: a new interpretation for the Monterey Event. Nat. Commun. 11 (1), 134. https://doi.org/10.1038/s41467-019-13792-0.

Sprain, C.J., Renne, P.R., Vanderkluysen, L., Pande, K., Self, S., Mittal, T., 2019. The eruptive tempo of Deccan volcanism in relation to the Cretaceous-Paleogene boundary. Science 363 (6429), 866–870. https://doi.org/10.1126/science.aav1446.

Stefano, C.J., Mukasa, S.B., Cabato, J.A., 2019. Elemental abundance patterns and Sr-, Nd- and Hf-isotope systematics for the Yellowstone hotspot and Columbia River flood basalts: bearing on petrogenesis. Chem. Geol. 513, 44–53. https://doi.org/10.1016/j.chemgeo.2019.03.012.

Stelten, M.E., Cooper, K.M., Vazquez, J.A., Reid, M.R., Barfod, G.H., Wimpenny, J., Yin, Q., 2013. Magma mixing and the generation of isotopically juvenile silicic magma at Yellowstone caldera inferred from coupling ^{238}U–^{230}Th ages with trace elements and Hf and O isotopes in zircon and Pb isotopes in sanidine. Contrib. Mineral. Petrol. 166 (2), 587–613. https://doi.org/10.1007/s00410-013-0893-2.

Streck, M.J., Ferns, M.L., McIntosh, W., 2015. Large, persistent rhyolitic magma reservoirs above Columbia River Basalt storage sites: the Dinner Creek Tuff Eruptive Center, eastern Oregon. Geosphere 11 (2), 226–235. https://doi.org/10.1130/GES01086.1.

Streck, M.J., Swenton, V.M., McIntosh, W., Ferns, M.L., Heizler, M., 2023. Columbia River Rhyolites: age-distribution patterns and their implications for arrival, location, and dispersion of continental flood basalt magmas in the crust. Geosciences (Switzerland) 13 (2). https://doi.org/10.3390/geosciences13020046.

Tian, X., Buck, W.R., 2022. Intrusions induce global warming before continental flood basalt volcanism. Nat. Geosci. 15 (5), 417–422. https://doi.org/10.1038/s41561-022-00939-w.

Tolan, T.L., Martin, B.S., Reidel, S.P., Anderson, J.L., Lindsey, K.A., Burt, W., 2009. An introduction to the stratigraphy, structural geology, and hydrogeology of the Columbia River Flood-Basalt Province: a primer for the GSA Columbia River Basalt Group field trips. In: Volcanoes to Vineyards: Geologic Field Trips Through the Dynamic Landscape of the Pacific Northwest.

Vervoort, J.D., Blichert-Toft, J., 1999. Evolution of the depleted mantle: Hf isotope evidence from juvenile rocks through time. Geochim. Cosmochim. Acta 63 (3–4), 533–556. https://doi.org/10.1016/S0016-7037(98)00274-9.

Washington State Department of Natural Resources, 2010. Digital Geology of Washington State at 1:100,000 Scale, Version 3.0.

Westerhold, T., Marwan, N., Drury, A.J., Liebrand, D., Agnini, C., Anagnostou, E., et al., 2020. An astronomically dated record of Earth's climate and its predictability over the last 66 million years. Science 369 (6509), 1383–1387. https://doi.org/10.1126/science.aba6853.